Structure–activity relationships, product species distribution and the mechanism of effect of multi-component flue gas on Hg^0 adsorption and oxidation over CuO/ACs†

Li Tong,‡[a] Penglai Zuo,‡[a] Xiaoxi Zhang,[a] Quanming Liang,[a] Kun Wang,[a] Yawen Yang,[a] Jieyu Liu,[a] Haixin Guo [iD] *[b] and Peng Zhang*[c]

A series of Cu-doped activated cokes (CuO/ACs) were synthesized *via* an impregnation method and applied for the removal of elemental mercury (Hg^0). Structure–activity relationships between Hg^0 removal and CuO/AC surface characteristics were identified. Hg^0 removal over CuO/AC occurs through a combination of physisorption and chemisorption and is mainly dominated by chemisorption. It was found that 1 nm micropores facilitate Hg^0 physisorption. Hg^0 could weakly adsorb onto an O-terminated crystal layer, whereas strongly adsorb onto Cu-terminated single highly dispersed, clustered and bulk CuO (110) crystal planes *via* the Mars–Maessen mechanism. Product distributions and mechanisms of Hg^0 adsorption and oxidation over the CuO/AC catalyst under multi-component flue gases are also discussed. O$_2$ enhances both physisorption and chemisorption toward Hg^0 by 38%. Inhibition of Hg^0 removal by SO$_2$ originates from the competitive adsorption and deactivation of CuO cation vacancies, whereas the impact is weakened by O$_2$ through generating 20% of physically adsorbed mercury product species. NO and O$_2$ promote Hg^0 chemisorption efficiency by 93% to form Hg(NO$_3$)$_2$. HOCl and/or Cl$_2$ produced by HCl can oxidize 100% of Hg^0 to HgCl$_2$, and the catalytic oxidation efficiency is approximately 29%, but O$_2$ slightly lowers the Hg^0 catalytic oxidation efficiency by 8%. The affinity ability between various flue gases and Hg^0 follows the order O$_2$ < NO < HCl.

1. Introduction

Mercury derived from fuel combustion has aroused wide concern owing to its unique chemical properties and has adverse effects on human health.[1] Among the various mercury species, elemental mercury (Hg^0) is the hardest to capture using currently available pollution control devices.[2,3]

Numerous efforts have been undertaken for mercury removal by means of adsorption and oxidation, which proved to be helpful for controlling Hg^0.[4–7] To date, wet flue gas desulfurization (WFGD) has been regarded as an effective way for disposing SO$_2$ and is adopted to remove Hg^{2+} after the oxidation of Hg^0 in industry. However, the re-emission of mercury during

the WFGD progress is a serious problem. Activated carbon injection (ACI) has been recognized as the mainly commercialized technology to remove mercury in the commercial application of coal-fired power plants, especially for activated carbons impregnated with halogen.[8] However, several shortcomings, such as carbon consumption, larger occupied area and higher costs, hamper its practical applications. In recent years, the use of transition metal oxides as oxidants for heterogeneous Hg^0 removal has been a growing field.[9,10] Nevertheless, it is difficult to remold the existing flue gas flow control devices, and catalysts' mechanical strength should be high enough to avoid dust erosion. For this purpose, materials could be employed downstream from fabric filters or electrostatic precipitators where temperature is commonly less than 160 °C.[8]

Among the various low-cost transition metal catalysts, copper oxides have been most developed because of their high activity for multi-pollutants, such as SO$_2$, NO and VOCs.[11–13] However, pure CuO is almost inert to Hg^0 removal. Therefore, Cu-based catalysts were employed to enhance Hg^0 removal performance (see Table S1 in the ESI†).[14–16] For example, Zhang *et al.*[14] studied Hg^0 adsorption over novel copper-based porous metal–organic

[a]*Institute of Urban Safety and Environmental Science, Beijing Academy of Science and Technology, Beijing 100054, China*

[b]*Agro-Environmental Protection Institute, Ministry of Agriculture and Rural Affairs, Tianjin 300191, China. E-mail: haixin_g@126.com*

[c]*National Center for Occupational Safety and Health, National Health Commission of the People's Republic of China, Beijing 102308, China. E-mail: zhangpengbd@163.com*

† Electronic supplementary information (ESI) available. See DOI: https://doi.org/10.1039/d4ra02483d

‡ Co-first author: Li Tong and Penglai Zuo contributed equally to this work.

frameworks (Cu-MOFs) with a chlorine-rich functional group and found that the resulting adsorbent had an Hg^0 removal efficiency of 91.8% at 120 °C in an N_2 atmosphere. Liu et al.[15] indicated that $CuO/g-C_3N_4$ materials had the Hg^0 removal efficiency exceeding 98.0% at 120 °C in an N_2 atmosphere. As a result, the Hg^0 removal performances over the Cu-based catalysts significantly vary in support. The active coke (AC), which is a common carbon-based material and has the characteristics of activated carbon, is typically considered a good candidate support for Hg^0 removal at low temperatures due to the lower expense and excellent mechanical strength.[17] Zhao et al.[16] investigated the effects of various synthesis factors on HNO_3 plus copper-modified ACs for Hg^0 removal. Still, the crystal structure affecting the mercury removal performance has not been studied in detail. CuO supported on the AC as a material system for Hg^0 removal had ever been demonstrated to be active for Hg^0 removal by fewer researchers, but little attention had been paid to the occurrence state and shape of the copper element and the detailed bonding sites for Hg^0 to reveal the structure–activity relationship between Hg^0 removal performance and CuO/AC surface characteristics.

Actually, the pollutants' removal performance is a result of the interaction among pollutants, materials, and the co-existing flue gas. In particular, Hg^0 is inferior in the gas volume and dipole moment, thus the removal performance is not mass transfer favored under the multi-component flue gas. Therefore, the Hg^0 removal selectivity strongly depends on the reciprocal effect of the material structures and flue gas components. The flue gas composition is primarily determined by the coal matrix and significantly affects the Hg^0 removal efficiency, particularly for O_2, SO_2, NO, and HCl. Laboratory experiments indicated that O_2 or HCl showed enhancement in Hg^0 oxidation.[18,19] However, the impact of NO or SO_2 on Hg^0 removal has not reached a consensus,[19–21] which mainly depends on the synthetic effect of competitive adsorption, poisoning and the newly generated active groups responsible for Hg^0 removal. However, the information on the internal reaction mechanism of Hg^0 and multi-component flue gases over CuO/AC was still insufficient for Cu-based AC catalysts.

Based on the above-mentioned statement, this work focuses on building the structure–activity relationship between Hg^0 removal performance and CuO/AC surface characteristics, and investigates the effect of multi-component flue gas and product species distribution for Hg^0 adsorption and oxidation over the CuO/AC. Furthermore, the affinity ability between different flue gases and Hg^0 over the CuO/AC is discussed, and the probable reaction mechanisms are also proposed. In the present work, insights into the structure–activity relationships between the Hg^0 removal performance and the CuO/AC provide guidance for the improvement of the current preparation method. Furthermore, exploring the reaction mechanism facilitates Hg^0 removal through optimizing the proportion of flue gas components to enhance the Hg^0 removal selectivity, and then probing into the product species distributions facilitates the regulation of the migration direction of product species, which oriently improve the adsorption efficiency or the catalytic oxidation efficiency instead of merely improving the material structure.

2. Experimental

2.1. Material preparation

The cylinder-shaped support with a diameter of 8 mm is a kind of commercial activated coke. The preparation procedure is as follows:

(1) Prior to use, virgin ACs were ground and crushed to 40–80 mesh. Afterwards, they were washed and rotated with distilled water and quickly dried at 110 °C for 14 h.

(2) Then, the CuO/ACs were synthesized by an equivalent-volume impregnation method with cupric nitrate as the precursor. The ACs were added into a solution with a required amount of cupric nitrate with the assistance of an ultrasonic cleaner for 0.5 h.

(3) Finally, the materials were dried at 110 °C for 14 h, followed by calcination under an Ar atmosphere at 300 °C for 3 h.

The catalyst is named M% CuO/AC, where M represents the mass ratio of copper oxide to AC.

2.2. Characterization

The samples' porosity characteristics were obtained using the nitrogen (N_2) adsorption–desorption method (Autosorb iQ, Quantachrome). Before measurement, all the CuO/ACs were outgassed at 120 °C for 12 h. X-ray diffraction (XRD) measurements were carried out using a powder diffractometer (Rigaku D/Max-RA). An ESCALAB 250 X-ray photoelectron spectrometer equipped with a monochromatic Al Kα source was employed to determine the elemental chemical states of the materials. Temperature Programmed Reduction (TPR) profiles of the samples were collected using an ASAP ChemiSorb 2920.

The technique of temperature-programmed desorption coupled with a Hg^0 analyzer (Hg^0-TPD) was used to analyze the adsorbed mercury product species and its amount on the catalysts. After the materials were placed in a Hg^0-containing gas flow for 2 h, the desorption process was recorded from 40 °C to 600 °C at a 10 °C min^{-1} heating rate in N_2.

2.3. Activity test

The removal performances of the samples were evaluated using a quartz microreactor, and the experimental device is referenced to our previous research.[20] Approximately 50 mg catalysts were used in each test. The reaction temperature is modulated through a heating furnace outside. A sealed Hg^0 permeation device was employed to provide a constant Hg^0 concentration. To shorten the experimental time, a higher initial Hg^0 concentration was chosen as 270 ± 5 μg m^{-3}. The Lumex RA-915M+ Hg^0 analyzer conventionally monitors the outlet Hg^0 concentration. The simulated flue gases at a total flow rate of 300 mL min^{-1}, consisting of NO, HCl, SO_2 or O_2, balanced in N_2 were accurately accommodated by the mass flowmeters. The weight hourly space velocity (WHSV) was calculated to be 3.6×10^5 mL g^{-1} h^{-1}. The pipeline was wrapped with heating tape to prevent Hg^0 deposition by heating the pipe temperature to 80 °C. To ensure equal experimental conditions, the CuO/AC catalyst was purged with N_2 for 20 min before each test. Moreover, a needle valve was added into the gaseous channel for the

determination of the initial Hg^0 concentration to eliminate the pressure drop caused by adding the CuO/AC samples to the empty quartz microreactor. In this work, we defined three terms: total removal efficiency, adsorption efficiency and catalytic oxidation efficiency, which were calculated based on the 2 h experimental results; it therefore referred to the cumulative efficiency. The cumulative total removal efficiency (η_{cap}) was calculated based on the difference in the integral area of inlet and outlet Hg^0, and the cumulative adsorption efficiency (η_{ads}) was calculated on the basis of the integral area of the Hg^0-TPD curve after pre-adsorption in a mercury-containing flue gas for 2 h. Therefore, the cumulative catalytic oxidation efficiency (η_{oxi}) is defined as (η_{cap}) − (η_{ads}). The breakthrough ratio of the samples is defined as follows:

$$\text{Breakthrough ratio} = \frac{C(Hg^0_{outlet})}{C(Hg^0_{inlet})} \times 100\% = \frac{C_{out}}{C_{in}} \quad (1)$$

where $C(Hg^0_{inlet})$ and $C(Hg^0_{outlet})$ denote the inlet and outlet Hg^0 concentrations of the fixed bed, respectively.

3. Results and discussion

3.1. Structure–activity relationship between the Hg^0 removal performance and the surface properties of CuO/AC

3.1.1. Hg^0 removal activity. The metal oxide loading value affects not only the aggregation and dispersion of materials but also its crystal structure and valence states.[22] Accordingly, the impact of Cu loadings on the Hg^0 removal was investigated. Fig. 1 illustrates the removal activity toward Hg^0 over the CuO/ACs with different CuO loadings in a N_2 atmosphere. It could be observed that the unmodified AC could hardly capture Hg^0, and there was also no removal of Hg^0 over pure CuO (data are not shown), but the activities continued to improve with the CuO content increasing to 20%. The results indicate that an intense interaction appears between the AC support and the active metal oxide component during the Hg^0 removal process. However, it was noted that the increment grew slightly when the Cu content ranged from 12% to 20%. Given both the cost and

the performance, the CuO loading values that appear in the following are set as 12%.

3.1.2. Effect of reaction temperature. Investigations on the reaction mechanism of 12% CuO/AC were performed as functions of temperature in the range of 60 °C to 180 °C with a constant gradient of 40 °C. As shown in Fig. 2, the activity toward Hg^0 reduced with the ascension of the temperature ranging from 60 °C to 180 °C. Three genres of catalytic oxidation, physisorption, and chemisorption can be defined to differentiate the removal mechanisms over various materials. Physisorption theory presumes that gaseous pollutants are preferential to diffuse to the material surfaces at lower temperature. The clear suppression in Hg^0 removal with the increase in temperature demonstrates that physisorption takes effect in the Hg^0 removal process over the 12% CuO/AC.

3.1.3. Effect of the physical property of CuO/ACs on the Hg^0 removal. To further identify the scope of physisorption, the N_2 adsorption–desorption isotherms and pore size distributions of CuO/ACs were recorded (see Fig. S1 in the ESI†), and merely part of the data are depicted in Fig. 3 to avoid the results indistinctly displayed. As can be seen, all the isotherms were indicative of a typical IV type with H4 hysteresis loops according to the IUPAC classification,[23] which suggests the presence of a mixture of narrow slit-like micropores and mesopores with irregular structures. Most pore sizes of all the catalysts were less than 2 nm. It should be noted that, after modification, an increase in CuO loadings to 12% enhanced the proportion for micropores distributing on 1 nm, but a further increase in the CuO content decreased the proportion. Therefore, it can be deduced that micropores centered at 1 nm may be a critical factor in determining the almost identical performance for 12% CuO/AC compared to that of catalysts with higher loadings. Table 1 summarizes the calculated structure parameters of AC with different CuO contents. It could be observed that AC support possessed the largest surface area and the well-developed porous fabric. However, the surface area and total pore volume followed a descending order as the CuO content increased. This appearance might occur on account of the fact
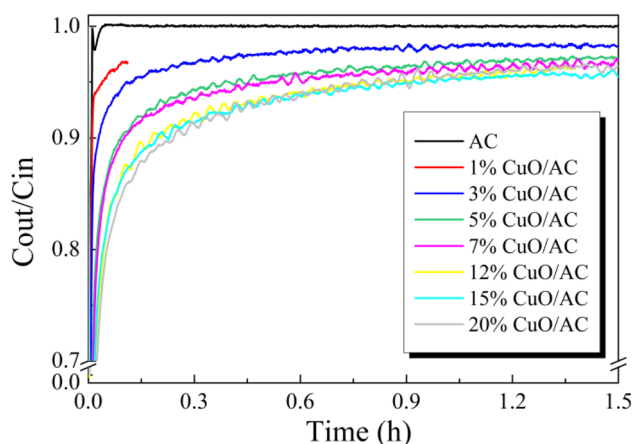

Fig. 1 Breakthrough curves of Hg^0 over virgin AC and CuO/AC with different CuO contents balanced in a pure N_2 atmosphere at 120 °C.

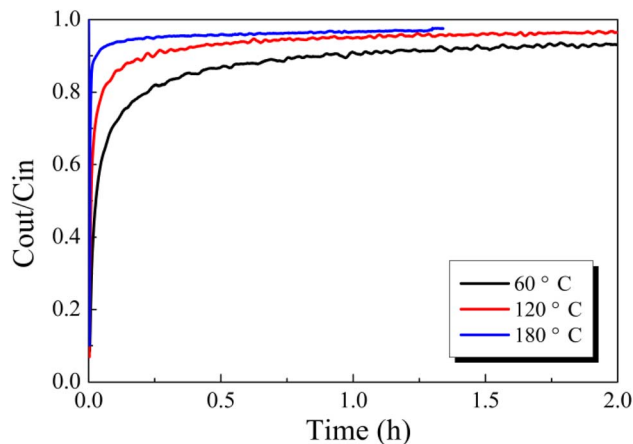**Fig. 2** Effect of reaction temperature on Hg^0 removal over 12% CuO/AC under a pure N_2 atmosphere.
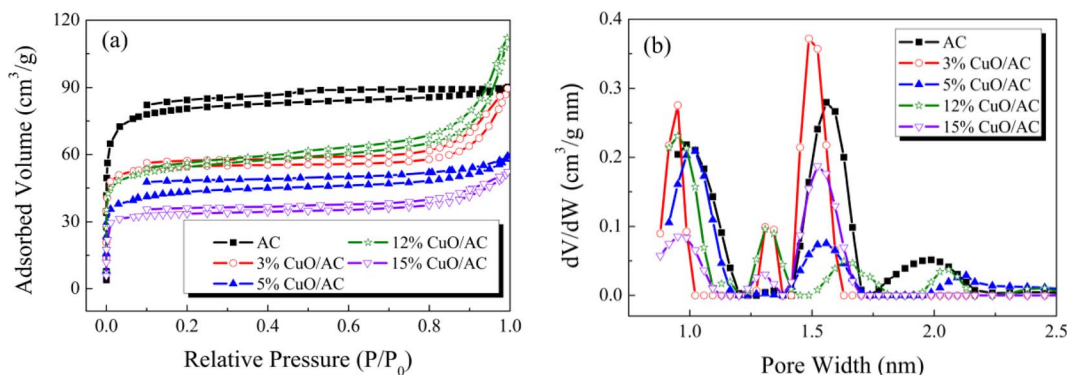
Fig. 3 (a) N_2 adsorption−desorption isotherms and (b) pore size distribution of the catalysts with different CuO contents.

Table 1 Structural parameters of CuO/AC with different CuO contents[a]

Samples	BET surface area ($m^2\ g^{-1}$)	Total pore volume ($cm^3\ g^{-1}$)	Average pore diameter (nm)
AC	251	0.138	2.20
1% CuO/AC	246	0.123	2.20
3% CuO/AC	193	0.131	2.72
5% CuO/AC	191	0.109	2.29
7% CuO/AC	160	0.102	2.71
12% CuO/AC	138	0.090	2.59
15% CuO/AC	121	0.077	2.56
20% CuO/AC	93	0.070	2.99

[a] The BET surface area was calculated from the N_2 adsorption isotherms using the BET equation. The total pore volume was accessed from the amount of N_2 adsorbed at $p/p_0 = 0.99$. The average pore diameter was calculated based on four times the total pore volume divided by the specific surface area.
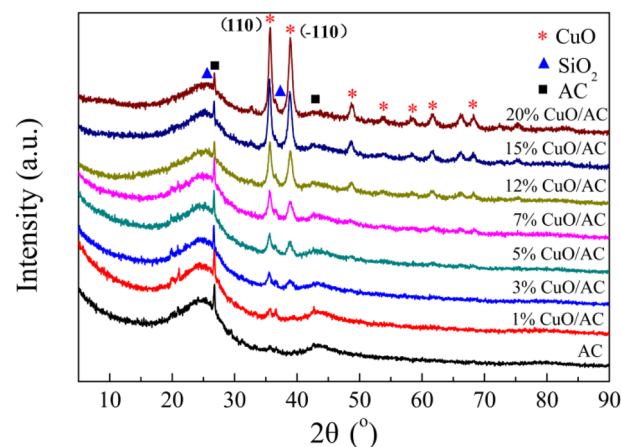
Fig. 4 X-ray diffraction patterns of CuO/AC catalysts with different CuO contents.

that CuO blocks into the pore channel of samples to cluster metal oxides augmented.[1] When the loading surpasses 12%, slit-like pores distributed on 1 nm are increasingly lessened.

Therefore, based on the comprehensive analysis above, it could be deduced that physisorption facilitates the Hg^0 removal but is not the only factor.

3.1.4. XRD analysis. As discussed, the removal mechanism toward Hg^0 is not solely dominated by physisorption. Thus, the chemical properties may be another governing factor for the performance of CuO/ACs. To reveal the occurrence state of the active species and corresponding crystal phases responsible for the Hg^0 activity, the XRD measurements of the CuO/ACs were carried out, as shown in Fig. 4. All reflections provided two typical diffraction peaks for the carbon matrix of AC support, which distributed on 26.78° and 43.38° (PDF# 89-8493), respectively, while the peaks at 25.65° and 36.60° (PDF# 82-1557) are attributed to SiO_2. With the introduction of metal oxides and carbon matrixes, SiO_2 peaks were still clearly observed; although all these peaks were less intense, this suggests that the crystallites of virgin AC have not changed because of the modification of metal oxides. In addition, new diffraction peaks at 35.58°, 38.99°, 48.77°, 53.90°, 58.52°, 61.61° and 68.28° (PDF# 80-1916) emerged and are matched to copper

oxide,[24,25] which therein (110) and (−110) crystal planes oriented preponderate. The diffraction peaks of the other phases were not detected. The result indicates that copper existed in the form of CuO phase for the CuO/ACs catalysts when calcined at 300 °C. Furthermore, doping metal oxides to AC shifted the diffraction peaks to a larger angle, implying that the CuO crystalline domains (shown in Table S2†) gradually grow according to the Scherrer formula,[26,27] which is likely related to the structural distortion of materials. As CuO contents ascend, the crystallinity of the active species becomes perfect, and that of grain diameters becomes bigger than the pores of the AC. Afterward, the CuO crystal particles deposit onto the surface of the AC and block the pores, which agrees with the BET analysis. The stacked CuO/AC catalysts probably further contribute to the nonuniform dispersion.

3.1.5. H_2-TPR analysis. Redox behaviors of the CuO/ACs were analyzed by H_2-TPR to further understand the enhancement effect of the AC modified by CuO active species for Hg^0 removal. As illustrated in Fig. 5, the virgin AC only exhibited one reduction peak located in 612 °C. This obvious peak is associated with the gasification of the AC support[28] and is also observed in 12% CuO/AC catalyst. After copper was added onto
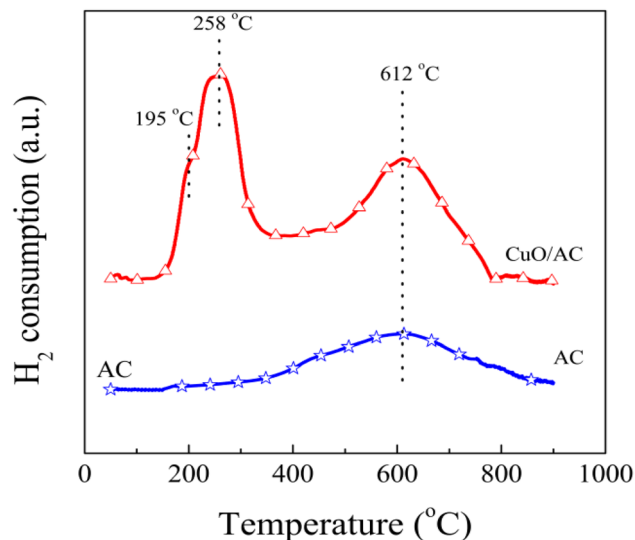
Fig. 5 H$_2$-TPR profiles of virgin AC and the 12% CuO/AC catalyst.

AC, another reduction peak appeared at 258 °C with a shoulder reduction peak at roughly 195 °C.

The environment of the copper ions and/or their structures is quite complicated and can be classified into two types of form: Cu^{2+}, including the isolated form (highly-dispersed) and clustered form (bulk-like), as well as Cu^{+}. However, the two peaks could not be explained through the step-wise reductions of the supported copper species, such as Cu^{2+} → Cu^{+} and Cu^{+} → Cu^{0}, because the areas for each peak are apparently distinct, and the reduction of Cu^{+} usually appears at high temperatures.[29] Moreover, many researchers[29,30] confirmed that most reduction of CuO occurred in a representative two-stage pattern at lower temperatures, where all the crystalline-supported Cu^{2+} ions reduce. Therefore, it can be concluded that the peak in the overlapped TPR profiles at 195 °C is associated with the reduction of the small two- and/or three-dimensional bulk CuO, weak magnetic associates, and isolated Cu^{2+} ions, whereas the peak centered at 258 °C corresponds to the reduction of large three-dimensional clusters of CuO and/or the bulk CuO phase. The lowering of reduction temperature evidences the redox ability of the supported copper oxide, which is greatly improved after modification. This is because the couple of Cu/Cu^{+} facilitates the reduction of the energy required for electron transport and/or boosts the mobility of the active oxygen, thus promoting the reactant activation and/or generation of surface oxygen vacancies.[31,32] The surface oxygen vacancies further result in structural distortion, which is in accordance with the XRD results.

3.1.6. XPS analysis. The structure–activity relationships between CuO/ACs and the Hg^{0} removal performance were further identified by analyzing the elemental chemical states and compositions before and after the reaction using XPS. The representative photoelectron profiles of O 1s, Cu 2p, and Hg 4f attaching to virgin and spent CuO/ACs are shown in Fig. 6. As depicted in Fig. 6(a), the O 1s profiles for virgin CuO/AC and spent CuO/AC samples were deconvoluted into three groups of

peaks. The sub-bands at a lower binding energy corresponded to the lattice oxygen (O$_\alpha$). The two sub-bands at a higher binding energy were ascribed to chemisorbed oxygen, weakly bonded oxygen or oxygen vacancies (O$_\beta$), and adsorbed water species or hydroxyl groups (O$_\gamma$).[31] The proportion of each branch of O 1s over the sample surface was obtained by calculating the homologous peak area. It was noteworthy that no obvious changes happened in the ratio of O$_\alpha$ while the content of O$_\beta$ decreased markedly from 79.70% to 61.27%; on the contrary, the ratio of O$_\gamma$ demonstrated an upward tendency from 2.01% to 20.37% after reactions. This result indicates that almost no difference is observed in the behavior of O$_\alpha$ after the reaction, whereas O$_\beta$ seems highly reactive and has dramatically been consumed after the reaction. Generally, the adsorption reaction would boost the transformation of valence states of catalysts, whereas the catalytic oxidation reaction just displays the opposite. Therefore, regarding CuO/AC, we infer that O$_\beta$ should be responsible for the redox reaction of mercury adsorption.

Fig. 6(b) presents the Cu 2p XPS spectra and their Gaussian fitting patterns of fresh and spent 12% CuO/AC samples. The Cu 2p profile was typically deconvoluted into four peaks, which could be assigned to Cu 2p$_{3/2}$, Cu 2p$_{1/2}$ and two satellite peaks. For the fresh 12% CuO/AC, the Cu 2p$_{3/2}$, Cu 2p$_{1/2}$ and two satellite peaks are the three primary characteristic peaks of Cu^{2+},[33] which echos the XRD and H$_2$-TPR results. However, after the adsorption of Hg^{0} onto the surface of CuO/AC, the Cu 2p$_{3/2}$ peak divided into two valence states. The binding energy in the range of 934.6–935 eV indicates the presence of CuO, while that centered at 933.8 eV is close to the Cu$_2$O peak,[25] demonstrating that CuO participates in removal progress and sectional species transform to Cu$_2$O after reaction. However, this result cannot exclude the simultaneous possibility of an adsorption behavior and catalytic oxidation during the Hg^{0} removal.

The Hg 4f XPS profiles of the spent 12% CuO/AC are shown in Fig. 6(c). A single peak centered at 103.3 eV in fresh 12% CuO/AC was ascribed to Si 2p and in line with the XRD results. After the reaction, an intense peak at 104.4 eV corresponding to Hg 4f$_{5/2}$ was attributed to HgO, and another small peak at 99.6 eV was assigned to Hg^{0}.[33] This result demonstrates that the mercury species over the spent CuO/ACs consists of Hg^{0} and HgO. Therefore, the results manifest that the Hg removal activities are restrained not only by the carbon texture, but also by the chemical properties, especially the lattice oxygen and chemisorbed oxygen groups.

3.2. Effect of multi-component gases and product species analysis

3.2.1. Effect of O$_2$. The Hg^{0} removal performances were evaluated at different O$_2$ concentrations. As displayed in Fig. 7, the initial breakthrough ratio of Hg^{0} promptly decreased to approximately 0.9 under pure N$_2$. Without O$_2$, the Hg^{0} bonds with lattice oxygen to generate weakly bonded MO$_{x-1}$–O–Hg species, physically adsorbs mercury species, and/or reacts with chemisorbed oxygen to form HgO through the Mars–Maessen mechanism.[34] Therefore, the decrease in CuO/AC activity is mainly because the surface oxygen is continually covered or
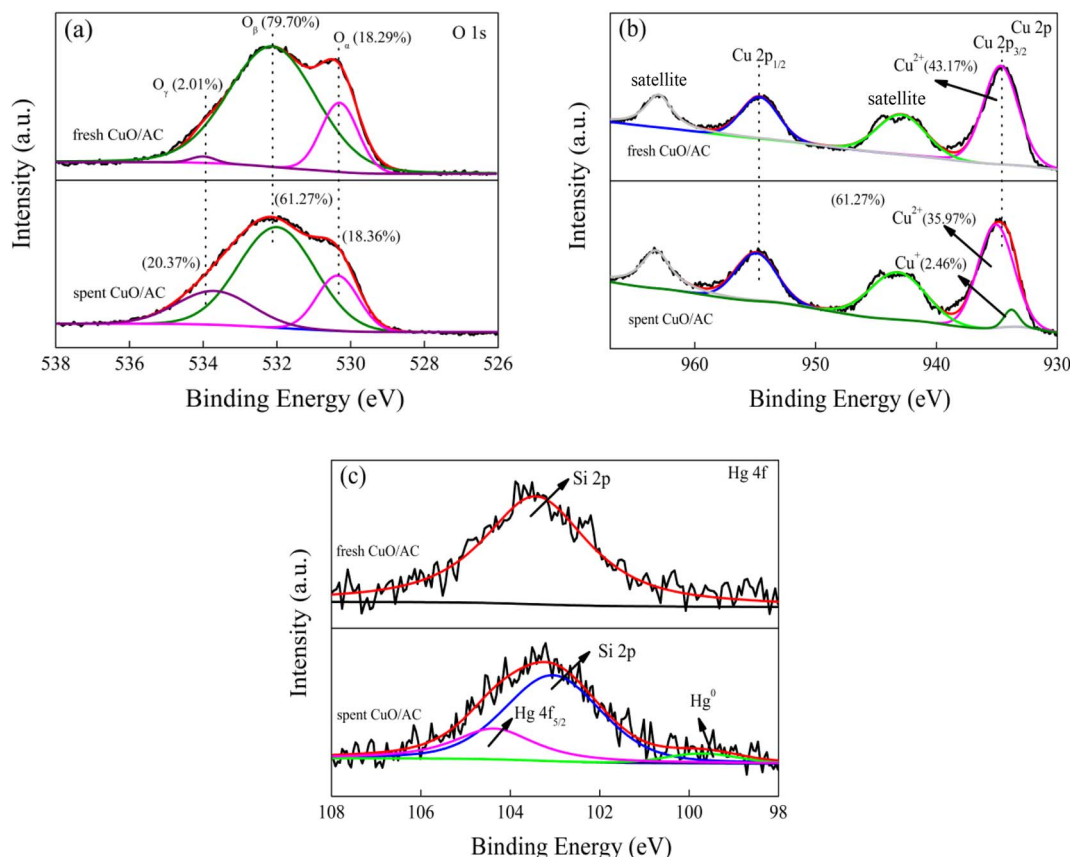
Fig. 6 (a) O 1s, (b) Cu 2p and (c) Hg 4f profiles of fresh AC and spent 12% CuO/AC catalysts.
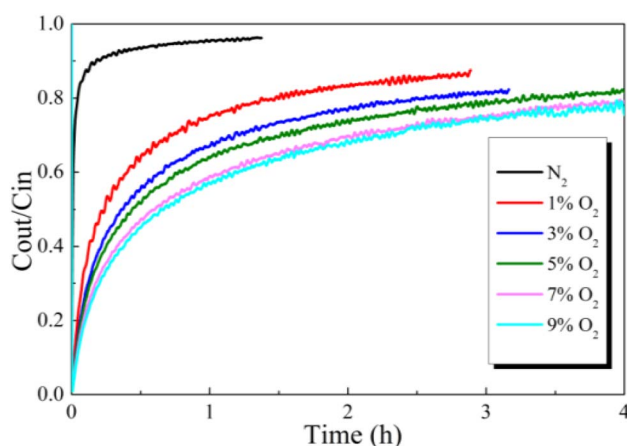

Fig. 7 Effect of O_2 concentration balanced in N_2 on Hg^0 removal over the 12% CuO/AC catalyst at 120 °C.

consumed. After a low level of O_2 flowed in, the Hg^0 removal rapidly increased, and improved step by step with the elevated O_2 content up to 9%. Nevertheless, no apparent increase was observed when the O_2 concentration surpassed 7%. Research by Li *et al.*[19] suggested that gas-phase O_2 could regenerate lattice oxygen or replenish chemisorbed oxygen over the catalysts, therefore exerting a promotional influence on Hg^0 removal. When the input O_2 achieves a specific content of 7%, gas-phase

oxygen and surface oxygen reach dynamic equilibrium over the 12% CuO/AC catalysts. Following that, the Hg^0 removal rate is almost of zeroth order with regard to the O_2 content. Thus, 7% is considered as the optimal O_2 concentration and will be used in the following experiments.

To reveal the reaction path toward Hg^0 removal under the O_2 atmosphere, the Hg^0-TPD profiles were collected. As shown in Fig. 8, irrespective of the presence of O_2, the Hg^0 decomposition peaks were in a similar position, beyond that the peak intensities were different. Therefore, it is inferred that the presence of O_2 will not alter the reaction path toward Hg^0 removal but will affect its removal efficiency. Two decomposition peaks appeared on the TPD spectra at around 144 °C and 178 °C. Nevertheless, after the samples were purged with N_2 for 1 h before the Hg^0-TPD experiments, the desorption peak vanished at a lower temperature (shown in Fig. 8(b)). Therefore, the peak at 144 °C was assigned to the decomposition of the physically adsorbed mercury species when combined with XPS characterization results, while that peak centered at 178 °C was assigned to the HgO desorption. The Hg^0-TPD profiles shown in Fig. 8(a) were further deconvoluted into two peaks based on the Gaussian method to distinguish the primary interaction mechanism, as shown in Fig. S2.† Interestingly, the area of HgO decomposition peak prevails regardless of the presence of O_2 in the pre-adsorption atmosphere, which suggests that chemisorption is the primary adsorption mechanism rather than physisorption.
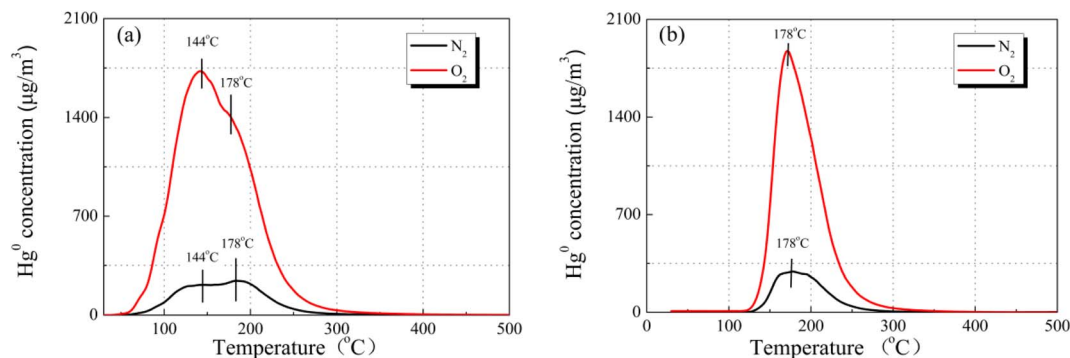
Fig. 8 Hg^0-TPD patterns of the 12% CuO/AC catalyst after pre-adsorption in an N_2 or O_2 atmosphere (a) without N_2 purge and (b) with N_2 purge at 120 °C (pre-adsorption reaction conditions: 7% O_2 and N_2 as the balance).

Previously, Xiang *et al.*[35] have also carried out similar research for the Hg^0 adsorption mechanism on the CuO (110) crystal planes to evaluate the applicability of the SCR system for Hg^0 removal. In their research, they found that Hg^0 could strongly adsorb onto the Cu-terminated CuO (110) crystal planes, whereas weakly adsorb onto the O-terminated crystal layer, and the former bonding way was predicted to be the main adsorption mode. Accordingly, their conclusions are well consistent with our results obtained in this work.

3.2.2. Effect of SO_2. The effects of various SO_2 atmospheres on the removal performance toward Hg^0 were investigated. As illuminated in Fig. 9(a), compared with the N_2 atmosphere, the addition of 200 ppm SO_2 significantly deteriorated the Hg^0 activity. An increase in the SO_2 concentration to 1000 ppm further marginally deteriorated the Hg^0 removal performance. A similar trend was also observed for the Hg^0 breakthrough curves by the addition of O_2, as exhibited in Fig. 9(b), indicating that SO_2 still shows inhibition in Hg^0 removal even when it coexists with O_2. However, the extent of the inhibitive effect is less intense with respect to that of the N_2 atmosphere. The SO_2 preponderates in the dipole moment and gas concentration, thus preventing Hg^0 collision onto the CuO/ACs surface through competitive adsorption. Furthermore, SO_2 exposed to metal oxides would react with active OH to generate metal

sulphate/sulphite, which destroys the surface cation vacancies of the metal oxides.[36] Despite in Section 3.2.1, it is proposed that adding O_2 could regenerate and/or replenish the active oxygen species, and the deterioration effect still cannot be eliminated. Accordingly, it is concluded that the consumption of reactive oxygen by the presence of SO_2 is not the essence for the decrease in Hg^0 removal performance because the O_2 content is ten times higher than that of SO_2, manifesting that catalytic oxidation does not occur under an O_2 atmosphere.

Desorption experiments were conducted to understand the Hg^0 removal mechanism after pre-adsorption in SO_2. As exhibited in Fig. 10, the Hg^0 decomposition peak appeared at approximately 142 °C. As previously reported,[37] the $HgSO_4$ desorption temperature was much higher than that of HgO. In comparison with the case of the O_2 atmosphere, we assume that the peak at 142 °C originates from the decomposition of physically adsorbed mercury species.

Therefore, it is demonstrated that the presence of O_2 weakens the suppression in physisorption toward Hg^0, but the chemisorption is completely constrained by the presence of SO_2. This result supports the above-mentioned viewpoint that the competitive adsorption between SO_2 and Hg^0 and the damage in the surface cation vacancies of the metal oxides take charge of the decrease in Hg^0 removal.
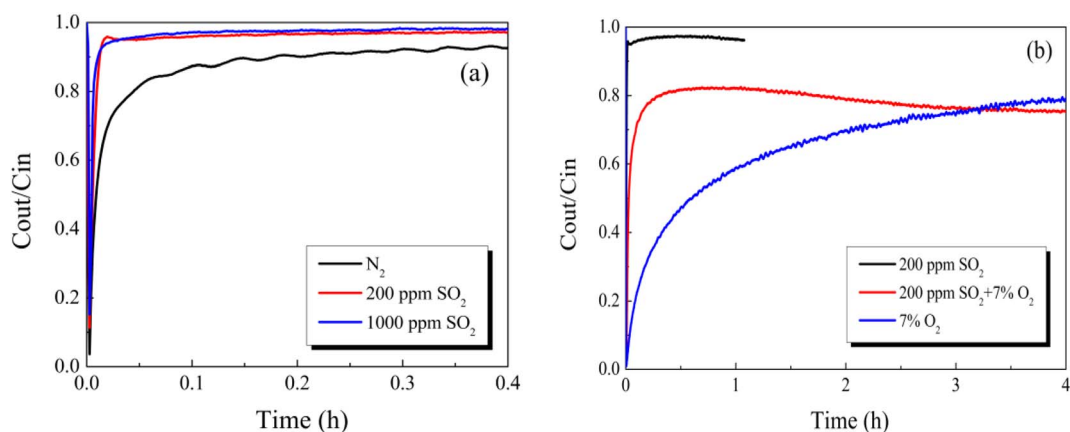

Fig. 9 Effect of SO_2 concentration balanced in an (a) N_2 or (b) O_2 atmosphere on Hg^0 removal over the 12% CuO/AC catalyst at 120 °C.

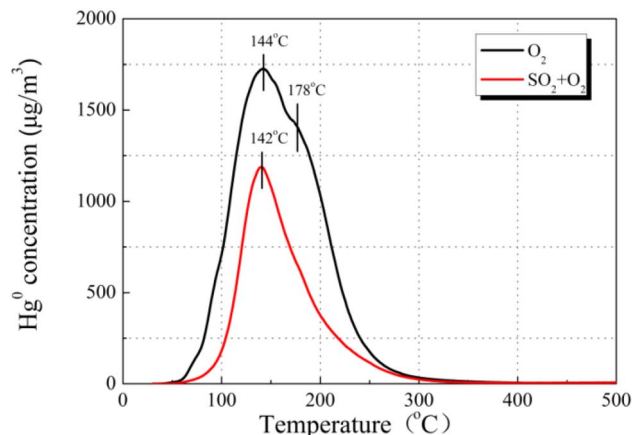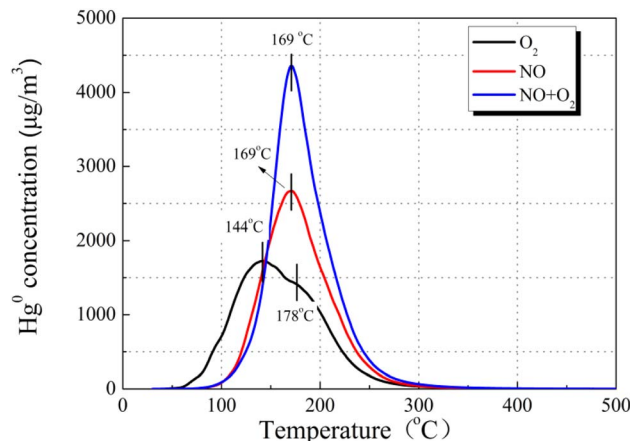**Fig. 10** Hg^0-TPD patterns of the 12% CuO/AC catalyst after pre-adsorption in SO_2 at 120 °C (pre-adsorption reaction conditions: 200 ppm of SO_2, 7% O_2, and N_2 as the balance).

Fig. 12 Hg^0-TPD patterns of the 12% CuO/AC catalyst after pre-adsorption in NO at 120 °C (pre-adsorption reaction conditions: 500 ppm of NO, 7% O_2, and N_2 as the balance).

3.2.3. Effect of NO. Fig. 11 explores the Hg^0 removal behaviors under different NO atmospheres over the CuO/AC catalyst at 120 °C. As observed, adding a low NO concentration of 100 ppm caused a rapid decrease in Hg^0 breakthrough ratio, steadily dropping with the increase in NO concentration to 500 ppm. *In situ* DRIFT characterization indicated that NO can cohere onto the metal oxides to form NO_2, NO^+ and NO_3^-,[38] and it is speculated that NO could occupy the C–O groups of activated coke/carbon surface to generate NO_2 groups *via* chemisorption,[39] thereinto NO_2 is an oxidant and can accept the outer electron of Hg^0, thereby promoting the oxidation. Moreover, researchers also affirmed that bidentate nitrate species might contribute to Hg^0 removal.[40] However, further increasing the NO concentration resulted in an increase in the Hg^0 breakthrough ratio. The NO could occupy the active sites for Hg^0 adsorption due to a much higher concentration than that of Hg^0, resulting in slight inhibition in Hg^0 removal. In addition, the NO_2 is postulated to react with Hg^0 to generate NO and HgO,[8] then it is possible that NO at a higher concentration drives the reaction left, reducing the removal activity.

Breakthrough experiments of Hg^0 over 12% CuO/AC were contrasted to identify the stimulative mechanisms for Hg^0 activity in the presence of NO. As demonstrated in Fig. 11, introducing O_2 into a NO atmosphere led to a prominent drop in the outlet Hg^0 concentration compared with that of an individual NO or O_2 atmosphere, indicating that the coexistence of O_2 and NO plays a synergistic role in the removal of Hg^0. The formed NO_2 species gradually increases after the O_2-containing gas was switched in, hence enhancing the Hg^0 removal over the CuO/ACs. Furthermore, the Hg^0 removal performance in NO obviously excels in that of O_2, which implies that the reaction paths for Hg^0 removal under O_2 and NO are different.

Accordingly, the Hg^0-TPD experiments were performed to clarify the mechanism after pre-adsorption in the presence of NO and O_2. As can be seen in Fig. 12, after pre-adsorption in the presence of NO, the positions of the primary Hg^0 desorption peaks were basically identical irrespective of the presence of O_2, suggesting the same mercury product species, whose temperature is lower than that of HgO decomposition. Taking account of the flue gas components, the desorption peak center
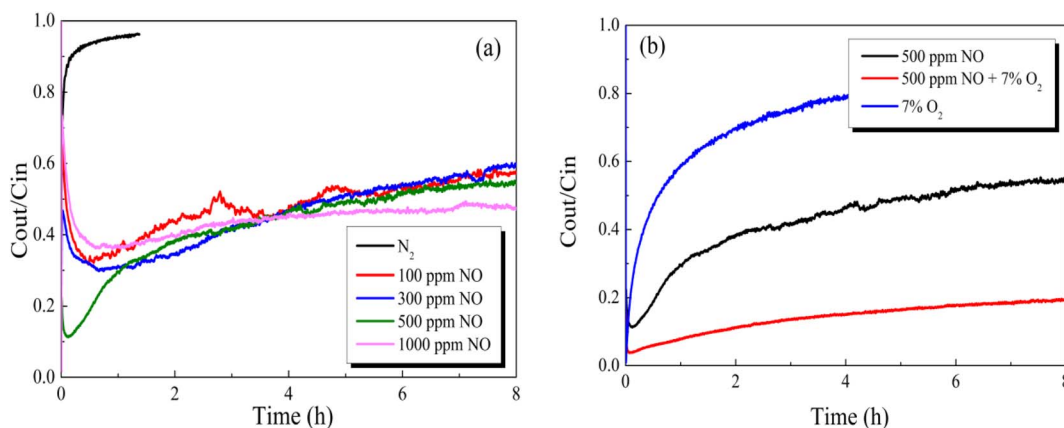

Fig. 11 Effect of NO concentration balanced in an (a) N_2 or (b) O_2 atmosphere on Hg^0 removal over the 12% CuO/AC catalyst at 120 °C.

temperature merely possibly corresponds to $Hg(NO_3)_2$ or HgO. Moreover, the $Hg(NO_3)_2$ decomposition temperature was lower than that of HgO.[41] Hence, the stable product species toward Hg^0 after pre-adsorption in NO is identified as $Hg(NO_3)_2$.

3.2.4. Effect of HCl. Further investigations on the effect of HCl on the removal performance toward Hg^0 over CuO/ACs were conducted. As depicted in Fig. 13, when 1 ppm HCl flowed in, the outlet Hg^0 concentration reduced gradually to zero after initially increasing and remained almost unchanged in the following 10 h. This appearance possibly stems from the initial active species such as atomic chlorine (HOCl)[42] insufficient to capture 100% Hg^0. As the newly formed HOCl species gradually accumulate, it increasingly promotes the Hg^0 removal. Consequently, the HCl must first adsorb onto the material surface before reacting with the Hg^0. It is also suggested that Cl_2 rather than HOCl can be produced to oxidize Hg^0 through the Deacon reaction,[43] which might contribute to the Hg^0 oxidation at lower temperatures. In addition, some researchers had indicated that the competitive adsorption reaction between HCl and Hg^0 occurred via a partial Deacon reaction,[11] but this phenomenon could be eliminated in the present work because increasing the HCl concentration will sequentially accelerate the removal of Hg^0 for the initial stages.

To better comprehend the nature of the interaction between HCl and Hg^0, we examined Hg^0-TPD patterns for CuO/AC after pre-adsorption in HCl at 120 °C. Fig. 14 displays the Hg^0 removal species after pre-adsorption in 15 ppm HCl regardless of the presence of O_2. The peaks after pre-adsorption in HCl and O_2 were observed at approximately 10 °C higher than the HCl-containing atmosphere, but the peak shape was extremely similar. As for the desorption characteristics of $HgCl_x$, it had been reported that Hg_2Cl_2 decomposition occurred in two steps, while $HgCl_2$ decomposition occurred at a single peak.[44] Therefore, $HgCl_2$ is the most plausible product formed after pre-adsorption in HCl, regardless of the presence of O_2. The peak shift should be attributed to the difference in bonding sites or molecular configuration between the Hg–Cu–Cl–O system on account of the O_2 atmosphere.

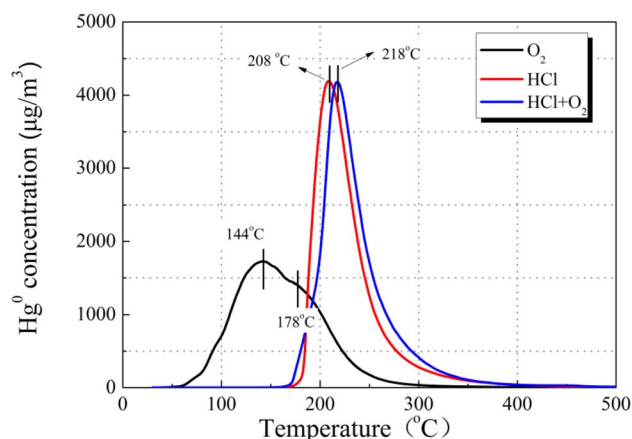**Fig. 14** Hg^0-TPD patterns of the 12% CuO/AC catalyst after pre-adsorption in HCl at 120 °C (pre-adsorption reaction conditions: 15 ppm of HCl, 7% O_2, and N_2 as the balance).

3.3. Distribution laws toward mercury removal species and proposed reaction mechanism

To comprehensively gain insights into the different flue gas components on distribution laws toward Hg^0 product species, the cumulative Hg^0 adsorption and oxidation efficiency was qualitatively calculated, and the results are shown in Fig. 15. As depicted, HCl was confirmed as the most effectual flue gas component contributing for Hg^0 removal, and the removal efficiency almost reached 100%. O_2 enhances Hg^0 adsorption by 38% compared to the N_2 atmosphere, while SO_2 and O_2 decrease Hg^0 adsorption by 24% compared to pure O_2. Under the coexistence of NO and O_2 atmospheres, 93% of Hg^0 was captured, showing the most outstanding enhancement in terms of Hg^0 adsorption, whereas the HCl atmosphere affords the most excellent enhancement by 29% for Hg^0 catalytic oxidation activity. The enhancement in cumulative Hg^0 removal efficiency under various flue gas components is sequenced: O_2 < NO < HCl, but this sequence is inversely proportional to their gas

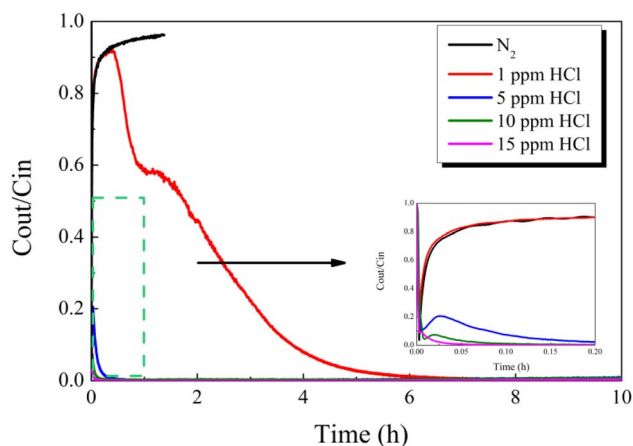**Fig. 13** Effect of HCl concentration balanced in N_2 on Hg^0 removal over the 12% CuO/AC catalyst at 120 °C.
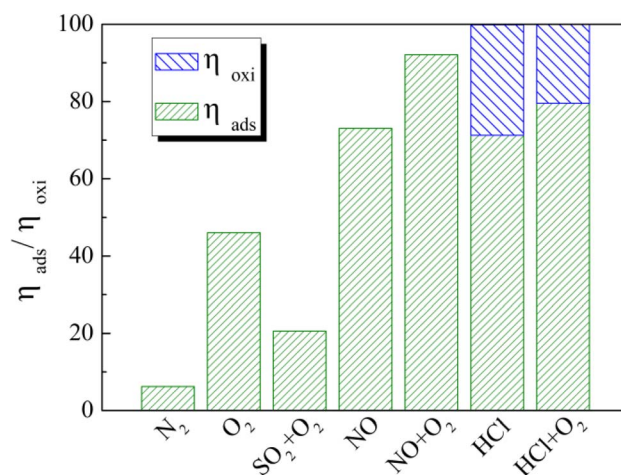

Fig. 15 Effect of individual flue gas components on Hg^0 adsorption and oxidation over the 12% CuO/AC catalyst at 120 °C.
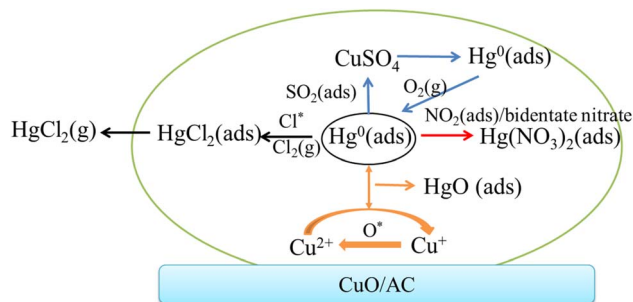
Fig. 16 Proposed removal mechanism toward Hg^0 under various simulated flue gases over CuO/AC.

concentration. As a result, we assume that the affinity ability rather than the gas concentration determines the removal activities toward Hg^0, which follows the same trend as that of the cumulative Hg^0 removal efficiency. This conclusion can be employed as a reference for adjusting the proportion of flue gas components to increase the removal selectivity toward Hg^0, further to improve the adsorption efficiency or the catalytic oxidation efficiency oriently.

Generally, the Hg^0 removal over the CuO/AC catalyst results from a combination of physisorption, chemisorption, and catalytic oxidation. The detailed Hg^0 removal mechanisms under various flue gases over the CuO/ACs catalyst are presented in Fig. 16.

First, the gaseous Hg^0 physically adsorbs onto the O-terminated CuO (110) crystal planes and chemically bonds onto the Cu-terminated highly dispersed, clustered and bulk CuO surface. Then, it reacts with chemisorbed oxygen to from HgO following the Mars–Maessen mechanism.

The presence of O_2 enhances both the chemisorption at the O_β sites and physisorption toward Hg^0 and the reaction is principally controlled by chemisorption through the generation of HgO. The competitive interaction between Hg^0 and SO_2, as well as the deactivation of cation vacancies of CuO leads to an inhibition in Hg^0 removal, whereas the presence of O_2 could weaken the damage by compensating the physically adsorbed mercury product species. In the presence of NO, the oxidizing NO_2 species and/or bidentate nitrate species formed on the metal oxide and carbon matrix are favorable for Hg^0 adsorption to produce $Hg(NO_3)_2$. In the presence of HCl, the generation of $HgCl_2$ over the CuO/ACs catalyst involves HOCl or Cl_2 oxidizing Hg^0, and a small brunch of that of $HgCl_2$ further escapes into the gas phase. The addition of the O_2 atmosphere to the HCl-containing gas causes a decrease in the Hg^0 oxidation efficiency.

4. Conclusions

CuO/ACs were prepared to remove Hg^0 at lower temperatures. It was found that 12% CuO/AC exhibits higher activity toward Hg^0 at 120 °C. Characterization techniques and bench-scale experiments were performed to gain insights into the structure–activity relationships, product species distribution law and the mechanism of impact of multi-component flue gases on Hg^0

adsorption and oxidation over the CuO/ACs. The main conclusions from this experimental study are summarised as follows:

• Hg^0 removal under a N_2 atmosphere over CuO/ACs is dominated by both physisorption and chemisorption, and it occurs primarily through chemisorption.

• Micropores centered at 1 nm facilitate the Hg^0 physisorption. The active component of the O-terminated CuO (110) crystal planes can physically adsorb Hg^0 and can chemically adsorb Hg^0 through the Mars–Maessen mechanism.

• The presence of O_2 enhances both physisorption and chemisorption of mercury by 38%, and the chemisorption occurring at the O_β sites preponderates with the product of HgO.

• Competitive adsorption and the deactivation of cation vacancies of CuO contribute to the decrease in Hg^0 removal by SO_2, whereas O_2 can weaken the deactivation by augmenting 20% of physically adsorbed mercury.

• NO and O_2 make for the Hg^0 chemisorption due to the generation of the NO_2 and/or bidentate nitrate species on the metal oxide or carbon matrix, and the removal efficiency reached 93%.

• The Hg^0 catalytic oxidation appears when HCl is converted into HOCl and/or Cl_2, but the catalytic oxidation efficiency of Hg^0 decreases in the presence of O_2 by 8%.

• The affinity abilities between various flue gases and Hg^0 are in the following order: $O_2 < NO < HCl$.

In future studies, it is recommended that quantum chemistry methods based on density functional theory (DFT) calculations be used to simulate the reaction progress further to identify the adsorption products under multi-component flue gases and clarify the interaction mechanism in heterogeneous systems. This suggestion will be addressed in the next work.

Data availability

The data that support the findings of this study are available from the corresponding author, Haixin Guo, upon reasonable request.

Conflicts of interest

There are no conflicts to declare.

Acknowledgements

References

1 L. Tong, W. Q. Xu, Y. Yang, R. H. Liu, Y. H. Wu and T. Y. Zhu, *RSC Adv.*, 2016, **6**, 78743–78749.

2 R. L. Hao, X. H. Dong, Z. Wang, L. Fu, Y. Han, B. Yuan, Y. P. Gong and Y. Zhao, *Environ. Sci. Technol.*, 2019, **53**, 8324–8332.

3 H. T. Zhao, X. Luo, J. He, C. Peng and T. Wu, *Fuel*, 2015, **147**, 67–75.

4 B. A. Dranga, L. Lazar and H. Koeser, *Catalysts*, 2012, **2**, 139–170.

5 R. L. Hao, Z. Wang, Y. P. Gong, Z. Ma, Z. Qian, Y. C. Luo, B. Yuan and Y. Zhao, *J. Hazard. Mater.*, 2020, **383**, 121135.

6 H. Zhao, C. I. Ezeh, S. Yin, Z. Xie, C. H. Pang, C. Zheng, X. Gao and T. Wu, *Appl. Catal., B*, 2020, **263**, 117829.

7 W. Xu, J. Pan, B. Fan and Y. Liu, *J. Cleaner Prod.*, 2019, **216**, 277–287.

8 Z. Q. Tan, J. Xiang, S. Su, H. C. Zeng, C. S. Zhou, L. S. Sun, S. Hu and J. R. Qiu, *J. Hazard. Mater.*, 2012, **239**, 160–166.

9 Y. Ma, B. Mu, X. Zhang, D. Yuan, C. Ma, H. Xu, Z. Qu and S. Fang, *Chem. Eng. J.*, 2019, **358**, 1499–1506.

10 B. Shen, S. Zhu, X. Zhang, G. Chi, D. Patel, M. Si and C. Wu, *Fuel*, 2018, **224**, 241–249.

11 W. Q. Xu, H. R. Wang, X. Zhou and T. Y. Zhu, *Chem. Eng. J.*, 2014, **243**, 380–385.

12 M. A. Fayad, A. M. Abed, S. H. Omran, A. A. Jaber, A. A. Radhi, H. A. Dhahad, M. T. Chaichan and T. Yusaf, *Int. J. Renewable Energy Dev.*, 2022, **11**, 1068–1077.

13 M. A. Fayad, S. I. Ibrahim, S. H. Omran, F. J. Martos, T. Badawy, A. M. Al Jubori d, H. A. Dhahad and M. T. Chaichan, *Fuel*, 2023, **331**, 125549.

14 Z. Zhang, J. Liu, Z. Wang and Y. J. Yang, *Fuel*, 2021, **289**, 119791.

15 D. J. Liu, C. Lu and J. Wu, *J. Nanopart. Res.*, 2018, **20**, 277.

16 B. Zhao, H. Yi, X. Tang, Q. Li, D. Liu and F. Gao, *Chem. Eng. J.*, 2016, **286**, 585–593.

17 Y. Xiao, D. Pudasainee, R. Gupta, Z. H. Xu and Y. F. Diao, *J. Hazard. Mater.*, 2017, **336**, 232–239.

18 H. Y. Wu, C. T. Li, L. K. Zhao, J. Zhang, G. M. Zeng, Y. e. Xie, X. N. Zhang and Y. Wang, *Energy Fuels*, 2015, **29**, 6747–6757.

19 H. L. Li, C. Y. Wu, Y. Li, L. Q. Li, Y. C. Zhao and J. Y. Zhang, *J. Hazard. Mater.*, 2012, **243**, 117–123.

20 K. L. Zhao, C. T. Li, S. H. Li, Y. Wang, J. Y. Zhang, T. Wang and G. M. Zeng, *Appl. Catal., B*, 2016, **198**, 420–430.

21 L. Tong, T. Yue, P. Zuo, X. Zhang, C. Wang, J. Gao and K. Wang, *Fuel*, 2017, **197**, 1–7.

22 Y. Wu, W. Xu, Y. Yang, J. Wang and T. Zhu, *Catal. Sci. Technol.*, 2018, **8**, 297–306.

23 D. Li, X. Tang, H. Yi, D. Ma and F. Gao, *Ind. Eng. Chem. Res.*, 2015, **54**, 9097–9103.

24 B. Zhao, H. Yi, X. Tang, Q. Li, D. Liu and F. Gao, *J. Hazard. Mater.*, 2019, **364**, 700–709.

25 W. Du, L. Yin, Y. Zhuo, Q. Xu, L. Zhang and C. Chen, *Fuel Process. Technol.*, 2015, **131**, 403–408.

26 M. Trépanier, A. Tavasoli, A. K. Dalai and N. Abatzoglou, *Appl. Catal., A*, 2009, **353**, 193–202.

27 L. K. Herrera, A. Justo and J. L. Perez-Rodriguez, *J. Nano Res.*, 2009, **8**, 99–107.

28 G. Q. Zhang, Z. Li, H. Y. Zheng, T. J. Fu, Y. B. Ju and Y. C. Wang, *Appl. Catal., B*, 2015, **179**, 95–105.

29 C. Liu, S. L. Nauert, M. A. Alsina, D. Wang, A. Grant, K. He, E. Weitz, M. Nolan, K. A. Gray and J. M. Notestein, *Appl. Catal., B*, 2019, **255**, 117754.

30 A. Kubacka, M. J. Munoz-Batista, M. Fernandez-Garcia, S. Obregon and G. Colon, *Appl. Catal., B*, 2015, **163**, 214–222.

31 L. Gao, C. Li, S. Li, W. Zhang, X. Du, L. Huang, Y. Zhu, Y. Zhai and G. Zeng, *Chem. Eng. J.*, 2019, **371**, 781–795.

32 T. Boningari, P. R. Ettireddy, A. Somogyvari, Y. Liu, A. Vorontsov, C. A. McDonald and P. G. Smirniotis, *J. Catal.*, 2015, **325**, 145–155.

33 L. Tang, C. Li, L. Zhao, L. Gao, X. Du, J. Zeng, J. Zhang and G. Zeng, *Fuel*, 2018, **218**, 366–374.

34 S. H. Qiao, J. Chen, J. F. Li, Z. Qu, P. Liu, N. Q. Yan and J. Q. Jia, *Ind. Eng. Chem. Res.*, 2009, **48**, 3317–3322.

35 W. Xiang, J. Liu, M. Chang and C. Zheng, *Chem. Eng. J.*, 2012, **200–202**, 91–96.

36 H. B. Fu, X. Wang, H. B. Wu, Y. Yin and J. M. Chen, *J. Phys. Chem. C*, 2007, **111**, 6077–6085.

37 M. A. Lopez-Anton, R. Perry, P. Abad-Valle, M. Díaz-Somoano, M. R. Martínez-Tarazona and M. M. Maroto-Valer, *Fuel Process. Technol.*, 2011, **92**, 707–711.

38 S. J. Yang, Y. W. Fu, Y. Liao, S. C. Xiong, Z. Qu, N. Q. Yan and J. H. Li, *Catal. Sci. Technol.*, 2014, **4**, 224–232.

39 L. Tong, W. Q. Xu, X. Zhou, R. H. Liu and T. Y. Zhu, *Energy Fuels*, 2015, **29**, 5231–5236.

40 Y. Yang, W. Xu, J. Wang and T. Zhu, *Fuel*, 2019, **249**, 178–187.

41 M. Rumayor, M. Diaz-Somoano, M. A. Lopez-Anton and M. R. Martinez-Tarazona, *Talanta*, 2013, **114**, 318–322.

42 A. Murakami, M. A. Uddin, R. Ochiai, E. Sasaoka and S. Wu, *Energy Fuels*, 2010, **24**, 4241–4249.

43 W. M. Chen, Y. Pei, W. J. Huang, Z. Qu, X. F. Hu and N. Q. Yan, *Environ. Sci. Technol.*, 2016, **50**, 2564–2572.

44 M. A. Lopez-Anton, Y. Yuan, R. Perry and M. M. Maroto-Valer, *Fuel*, 2010, **89**, 629–634.